ASAR polarimetric, multi-incidence angle and multitemporal characterization of Doñana wetlands for flood extent monitoring

Belen Marti-Cardona [a,*], Carlos Lopez-Martinez [b], Josep Dolz-Ripolles [a], Ernest Bladè-Castellet [a]

[a] Flumen Research Group, Dept. of Hydraulic, Maritime and Environmental Eng., Universitat Politècnica de Catalunya, UPC, Barcelona, Spain
[b] Remote Sensing Lab., Dept. of Signal Processing and Communications, Universitat Politècnica de Catalunya, UPC & Institut d'Estudis Espacials de Catalunya, IEEC-CRAE, Barcelona, Spain

ARTICLE INFO

ABSTRACT

Doñana National Park wetlands, in South West Spain, undergo yearly cycles of inundation and drying out. During the hydrological year 2006–2007, 43 ASAR/Envisat images of Doñana, mostly in HH and VV polarizations, were acquired with the aim to monitor the flood extent evolution during an entire flooding cycle. The images were ordered in the seven ASAR incidence angles, also referred to as swaths, to achieve high observation frequency.

In this study, backscattering temporal signatures of the main land cover types in Doñana were obtained for the different incidence angles and polarizations. Plots showing the σ^0HH/σ^0VV ratio behavior were also produced. The signatures were analyzed with the aid of miscellaneous site data in order to identify the effect of the flooding on the backscattering. Conclusions on the feasibility to discriminate emerged versus flooded land are derived for the different incidence angles, land cover types and phenological stages: intermediate incidence angles (ASAR IS3 and IS4) came up as the most appropriate single swaths to discriminate open water surface from smooth bare soil in the marshland deepest areas. Flood mapping in pasture lands, the most elevated regions, is feasible at steep to mid incidence angles (ASAR IS1 to IS4). In the medium elevation zones, colonized by large helophytes, shallow incidence angles (ASAR IS6 and IS7) enable more accurate flood delineation during the vegetation growing phase.

Since Doñana land covers require different observation swaths for flood detection, the composition of different incidence angle images close in time provides the optimum flood mapping. Such composition is possible four times per ASAR 35-day orbit cycle, using pairs of 12-h apart IS1/IS6 and IS2/IS5 Doñana images.

© 2010 Elsevier Inc. All rights reserved.

1. Introduction

Doñana National Park marshes lie on the colmated Guadalquivir River estuary, on the Spanish Atlantic coast (Fig. 1). Doñana is notable for the great diversity of its biotypes and constitutes a crucial passage and breeding site for hundreds of thousands of migratory birds each year (García-Novo & Marín-Cabrera, 2005).

In 1998 the Spanish Ministry of the Environment promoted the project called Doñana 2005 (Saura et al., 2001) aimed at the restoration of the marshes natural hydrologic scheme, deeply altered during most of the XX century (Menanteau, 1984). Within the frame of Doñana 2005 the Flumen Research Group, at the Universitat Politècnica de Catalunya, developed a hydrodynamic model of the marshes (Bladé & Gómez, 2006), in order to predict the wetland response to proposed actions in the Guadalquivir River basin. The rigorous calibration of the hydrodynamic model required observations of the marshes flood extent at different instants of the hydrologic year,

with higher temporal resolution during the rainfall period. In order to obtain these observations, 43 images of the Synthetic Aperture Radar sensor ASAR (European Space Agency, 2006), on board of the Envisat satellite, were acquired from September 2006 to July 2007. The images were acquired at six different incidence angles and most of them in HH and VV polarizations.

Radar systems have been used for wetland characterization since the 1970s. In addition to their day and night, and all-weather imaging capabilities, SAR systems can provide unique, valuable information on wetland biophysical parameters, such as soil and vegetation moisture (Kasischke et al., 2003; Pierdicca et al., 2010; Ulaby et al., 1986; Wickel et al., 2001), and vegetation structure and biomass (Dobson et al., 1992; Grings et al., 2005; Le Toan et al., 1992; Le Toan et al., 1997; Moreau & Le Toan, 2003; Ulaby et al., 1986). The radar signal is also capable to partially penetrate vegetation canopies and detect standing water underneath (Hess et al., 1990; Hess et al., 1995; Krohn et al., 1983; Martinez & Le Toan, 2007; Ramsey, 1998; Rosenqvist et al., 2002). Moreover, flatness of wetlands surface minimizes undesirable topographic effects on the radar returns. Five review articles (Henderson & Lewis, 2008; Ramsey, 1998; Schmullius & Evans, 1997; Kasischke et al., 1997 and Hess et al., 1990) considering 261

* Corresponding author. Campus Nord UPC, Jordi Girona 1 D1-208, 08034 Barcelona, Spain.
E-mail address: belen.marti@upc.edu (B. Marti-Cardona).

Fig. 1. Site location.

articles from 1965 to 2007 summarize most of the current knowledge concerning radar–wetland interactions. These reviews evidence the complexity of the SAR–wetland relationships, highly influenced by the structure and density of the vegetation in relation to the observation wavelength and incidence angle. Despite this complexity, some generally agreed conclusions of the reviewed papers are gathered as follows:

L-band is considered more appropriate than C and X-band for flood detection in forested wetlands (Bourgeau-Chavez et al., 2001; Costa et al., 1998; Hess et al., 1990; Hess et al., 1995; Wang et al., 1995). The L-band longer wavelength facilitates the penetration of the radar signal through the forest canopy and the interaction with the soil or water surface underneath, while X and C returns come primarily from branches and leaves. The latter wavelengths are better suited for flood mapping in herbaceous marshes (Costa et al., 1998; Kasischke et al.;, 1997; Pope et al., 1997; Ramsey, 1995). In general for all bands, steep incidence angles favor the radar signal penetration through the canopy, while increases in biomass or incidence angle intensify the signal–canopy interactions to the detriment of penetration (Costa, 2004; Costa et al., 1998; Grings et al., 2005; Hess et al., 1990; Ramsey, 1998). Subcanopy flood detection can be enhanced by the double bounce of the radar waves between trunks and water surface in forests (Hess et al., 1990; Kasischke et al., 1997; Martinez & Le Toan, 2007; Ramsey, 1998), and between vertical stalks and water surface in herbaceous wetlands (Grings et al., 2005; Grings et al., 2006; Kasischke et al., 2003; Parmuchi et al., 2002; Pope et al., 1997; Ramsey, 1998). Kandus et al. (2001) and Töyrä et al. (2001) suggested a combination of incidence angles: steep ones for subcanopy flooding detection and shallow angles to delineate open water, since wind-roughened water surface can be confused with emerged land at low incidence angles. Novo et al. (1998) also pointed at the interest of multi-incidence angle imagery to retrieve biophysical parameters of several macrophyte species in the Amazon. Temporal variability is inherent to most wetland environments. Some authors have advocated the importance of multitemporal imagery to capture the flood and vegetation temporal patterns, since this information is of great relevance for numerous fields of research and for efficient wetland

managing (Brown et al., 1996; Costa & Telmer, 2006; Henderson & Lewis, 2008; Kandus et al., 2001). An L-band imagery time series spanning 2 years was successfully analyzed by Rosenqvist et al. (2002) to model the spatial and temporal variation of inundation in the Central Brazilian Amazon. A 4-year long L-band set was used by Martinez and Le Toan (2007) to monitor the flood extent dynamics and spatial distribution of broad land cover types in the Amazon flood plain. Grings et al. (2005) utilized multitemporal C-band data to observe and model herbaceous vegetation growth in the Parana River Delta, Argentina. Töyrä and Pietroniro (2005) combined C-band SAR and optical data from 1996 to 2001 to derive a flood duration map of the Peace-Athabasca Delta, in Canada. Kasischke et al. (2003), used 22 C-band scenes over a 25-month period to monitor hydrologic conditions in South Florida wetlands. Nevertheless, despite the cited research, most studies assessing change in wetlands are restricted to image acquisition opportunities and fail to capture temporal patterns.

The present paper aims at the backscattering temporal character-ization of Doñana land cover types and determination of the viability of the ASAR scenes to monitor the marshes flood extent. To this aim, backscattering temporal signatures of Doñana main land cover types are obtained for HH and VV polarizations, and for six ASAR incidence angles. Polarimetric behavior of the signatures is analyzed with the aid of extensive site data and plausible explanations to the observed main backscattering features are suggested, based on the state of the art on radar–wetland interactions. Conclusions on the feasibility to detect flooding are extracted for the different swaths and polariza-tions. Since the distribution of land cover classes in Doñana is known (Cabezudo, 1979; Luque et al., 2005; Peinado et al., 1990; Rivas-Martínez et al., 1980), the analysis does not focus on the classes' spatial discrimination but on the effect of the inundation on each class backscattering characteristics.

Conclusions on flood mapping feasibility are used in a following study to delineate inundation in Doñana from the ASAR scenes. So far, such delineation has allowed observing the wind drag action on Doñana water bodies and the evaporation and infiltration losses rate (Ramos et al., 2009).

2. Study site

Doñana National Park is located in South West Spain, on the banks of the Guadalquivir River, near its mouth on the Atlantic Ocean coast. Approximately half of the Park extension, 27,000 ha, is marshland area. The marshes undergo a yearly cycle of inundation in autumn and drying out during the spring season, and its flood extension varies considerably among years depending on the precipitation (Bayán-Jardín & Dolz-Ripollés, 1995; Clemente et al., 2004; Rodríguez & Clemente, 2002).

The topography of the marshes is extremely flat, with a maximum elevation difference of 2.50 m and slope smaller than 1.3% in 98% of the area (Fig. 2). Despite its subtleness, the marshes topography has a critical effect on the hydroperiod or time that each zone remains flooded, which in turn determines the vegetal species growing in it (Aragones et al., 2005; Diaz-Delgado et al., 2006; García et al., 2005; Rodríguez-Ramirez & Clemente-Salas, 2002).

In broad outlines, Doñana marshes can be subdivided into three area types: paciles, ponds centers and transition zones, which are described below and sketched in Fig. 3.

The deepest marshland areas, the centers of ponds and water-courses, are the first ones in flooding and the last ones in drying out. In other words, they are the areas of longer hydroperiod. The centers of the ponds are formed by clayey bare soil, and virtually no vegetation develops in them at any time of the year (García et al., 2005).

The locally called paciles, the most elevated zones, are fluvio-tidal sediment bars located between ponds and watercourses (Rodríguez & Clemente, 2002). The paciles only flood in wet years, when the water level in the marshes rises high enough. The vegetation found in the
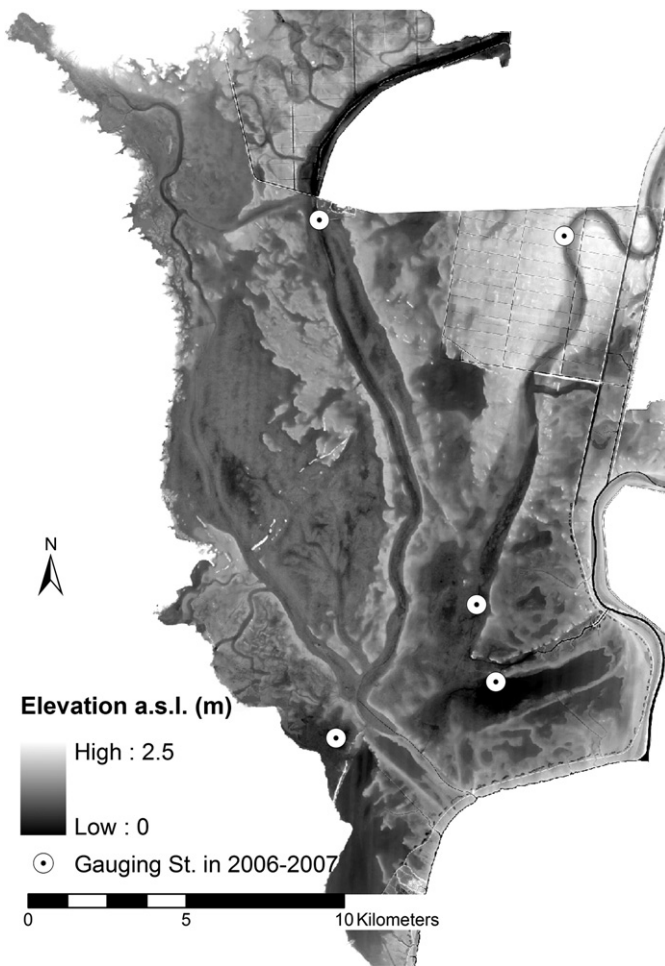
Fig. 2. Digital terrain model and location of the gauging stations.

paciles is pasture land known as almajar. The almajar is dominated by the almajo plant or *Arthrocnemun macrostachyum*, shrub of height between 0.5 and 1.1 m, and percentage of coverage around 50% (García et al., 2005). When flooded, the water depth in the paciles rarely exceeds 0.2 m, so most of the almajo bush remains out of the water.

The transition zones, between paciles and ponds centers, are colmated watercourses. They flood almost every year and communities of large helophytes develop in them. These communities are largely dominated by two species: *Scirpus maritimus* (Castañuela) and *Scirpus litorales* (Bayunco). The Castañuela is an herb of triangular cross-section and height ranging from 0.6 to 1.0 m. The Bayunco is reed-like, with circular cross-section, and often higher than 1.0 m. Both species start emerging from the water surface towards the end of February. They experience rapid growth throughout the spring season and in April and May form dense vegetation masses reaching 95% of

surface coverage (García et al., 2005). The Castañuela and the Bayunco dry out and die during the summer. Their brown stems stick out of the water surface when the marshes flood in autumn, but they progressively putrefy and sink by the spring.

As revealed by the description above, Doñana's landscape is highly dynamic in time and space: in fall, the first rainfall events can flood thousands of hectares in a few days. From the radar point of view, the water bodies' appearance changes considerably with the wind due to the wind-induced surface roughness. The wind speed in Doñana has been observed to follow daily patterns and the water surface roughness to be spatially quite variable. During the first 2 to 3 months of the inundation period, dry plants from the previous hydrologic cycle still emerge from the flooded surface and introduce some effect in the water backscattering coefficient. This effect fades out as the dry plants decay and disappear. In spring new green vegetation starts emerging in the transition zones and covers the water surface in a couple of months. The flooded vegetation shows high backscattering in virtue of the double bounce effect of the radar waves. Also throughout the spring season, the flood extent recedes gradually until the marshes dry out completely in June or July.

3. Experimental data

3.1. Study period

This study focuses on the hydrologic year 2006–2007 (from September 2006 to August 2007), because it was a wet year in which the paciles flooded partially, and also because continuous series of water level and meteorological data were registered at Doñana gauging stations (Figs. 2 and 4).

3.2. ASAR imagery

Forty-three ASAR images of Doñana marshes were acquired in Alternating Polarization mode (ASA_APG_1P product) from September 2006 to July 2007. The ASAR sensor is installed on board of the Envisat satellite of the European Space Agency (European Space Agency, 2006). ASAR is a synthetic aperture radar sensor using C-band (5.34 GHz) and has a spatial resolution of approximately 30 m × 30 m when operating in the Alternating Polarization mode. In this mode, ASAR acquires images in two of the three polarization channels as follows: HH, VV and HV. In the HH and VV channels the sensor antenna operates respectively in horizontal or vertical linear polarization, and the same polarization is used for transmitting and receiving. In the HV channel, transmission and reception consider different polarizations. ASAR's imaging swath can be selected by changing the beam incidence angle. There are seven predetermined swaths designated as IS1 to IS7. Table 1 shows the incidence angle range for each swath.

Detailed observation of the filling process is of particular interest for the calibration of the hydraulic model. This process is rapid and coincides with overcast weather. These two characteristics pointed at the ASAR instrument as the most suitable sensor for monitoring
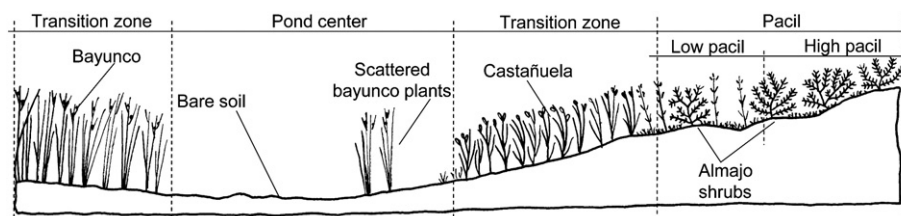

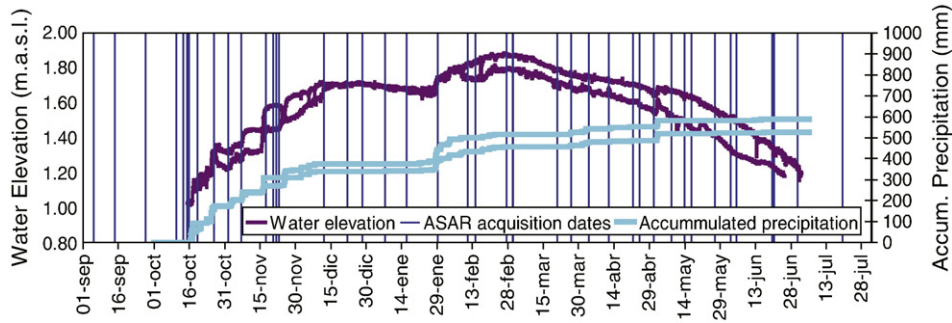**Fig. 3.** Ideal cross-section of the marshes. Adapted from García et al. (2005).

Fig. 4. Water elevation and cumulated precipitation in two gauging stations, and image acquisition dates during the hydrologic year 2006–2007.

Doñana's inundation: microwave radiation can penetrate clouds and ASAR's pointable capability enables up to 14 image acquisitions of Doñana per 35-day orbit cycle.

Fig. 4 shows the ASAR image acquisition dates during the study period together with the cumulated precipitation and water level evolution in Doñana at different gauging stations. The images were ordered in the seven ASAR incidence angles to achieve high temporal resolution, especially during the fall, when the marshes rapidly fill with water. Ascending and descending tracks were used indifferently, in virtue of the terrain flatness and the azimuthal isotropy of the vegetation. Phase data were discarded due to the incoherency between ASAR polarization channels and between different acquisition dates on distributed targets. The Alternating Polarization mode and the polarization configuration for each image acquisition were chosen in accordance with previous work assessing ASAR's suitability for monitoring Doñana marshes (Martí-Cardona et al., 2006).

The number of image acquisitions per swath is summarized in Table 1. Swath IS5 experienced technical irregularities during the study period, so it has not been used in this study.

3.3. Hydrometeorological data

A network of five permanent hydrometeorological gauging stations was installed in September 2004 (Fig. 2). These stations acquire 10-min records of water level, water temperature, conductivity, dissolved oxygen, rainfall, wind direction and velocity, air temperature and humidity, soil temperature and incident and reflected visible and near infrared radiation (Ramos et al., 2009).

3.4. Digital terrain model

In September 2002 a LIDAR survey flight was conducted over Doñana marshes. The LIDAR data set was used to generate a digital terrain model (DTM) of 2.00 m² and 0.15 m planimetric and elevation resolution respectively (Fig. 2; Ibáñez & Gili-Ripoll, 2008).

Table 1
ASAR swaths incidence angle ranges in Alternating Polarization mode, and number of image acquisitions per swath and polarization during the 2006–2007 hydrologic year.

ASAR swath	Incidence angle range	Number of images	Polarization
IS1	15.0–22.9	5	4 in HH/HV 1 in HH/VV
IS2	19.2–26.7	6	HH/VV
IS3	26.0–31.4	8	2 in HH/HV 6 in HH/VV
IS4	31.0–36.3	8	HH/VV
IS5	35.8–39.4	3 (not used)	HH/VV
IS6	39.1–42.8	9	HH/VV
IS7	42.5–45.2	7	HH/VV

3.5. Field data

Ground truth data were collected coinciding with ASAR image acquisitions over Doñana. These data consisted of eight approximately 8 km long transects with 100 m spaced sampling points. Flood stage, percentage of water, soil and vegetation coverage, and vegetation structure were recorded at the sampling points. Other ancillary data used in this study were Landsat images and flood maps derived from them (Aragonés et al., 2005; Bustamante et al., 2009), and vegetation thematic maps (Luque et al., 2005).

4. Methods

4.1. Image calibration

All the images were received from ESA as radar brightness (i.e., elevation, antenna pattern and range spreading loss corrected but with no elevation angle compensation), and georeferenced. To perform the absolute image calibration and derive the radar backscattering coefficient σ^0 the following expression was applied at each image pixel (Rosich & Meadows, 2004):

$$\sigma^0 = \frac{DN^2}{K}\sin(\alpha)$$

where:

- $K =$ absolute calibration constant, delivered for each image and polarization by ESA;
- $DN^2 =$ pixel intensity value;
- $\alpha =$ local incidence angle at each pixel.

For applying this calibration flat terrain was assumed, i.e., the increment of incidence angle due to the terrain slope was neglected. The maximum σ^0 error introduced by this simplification was assessed, being of 5% in areas with slope higher than 1.3% (less than 2% of the marshes extent) at IS1 images. The error decreases below 1% for the same areas at IS7 images.

4.2. ROIs definition

Once the images were calibrated, 15 regions of interest (ROIs) representative of the main land cover types in Doñana were defined. These ROIs included roughly 1000 pixels each (15.6 ha), and were selected so that they are composed of approximately flat areas with homogeneous vegetation. The definition of the ROIs was as follows:

- Three out of the 15 ROIs are located in the ponds centers and characterize the land cover class designated as *Deep Bare Soil*.
- Seven ROIs were defined in the transition zones. Four of them correspond to communities dominated by the Castañuela, and characterize the class called *Castañuela*. The Bayunco is the main

vegetation species found in the other 3 ROIs, which represent the class *Bayunco*.

- Five ROIs are located in the paciles. Two of them were defined in areas of almajar that flooded during the study period and have been designated as *Low Pacil*. The other 3 occupy slightly higher areas which did not flood and represent the class *High Pacil*.

The ROIs homogeneity was checked at every image by ensuring that the ROIs intensity distribution agreed with the Gamma theoretical one for uniform targets. This was almost always the case except on a few cases, at the beginning of the Bayunco emergence, when plants can start patching the water surface unevenly.

4.3. Determination of the ROIs flooding period and backscattering signature

Ground truth data plus the DTM and the water level records were used to determine the dates on which the different ROIs flooded and unflooded during the study period. Given the extent of the ROIs (about 15 ha), they can take a few days to flood or emerge completely. The beginning and end of the flooding period were selected as the dates on which 50% of the ROIs surface was under water, that is, as the dates on which water elevation records nearby each ROI reached the ROI's terrain median elevation.

The backscattering coefficient arithmetic mean of the pixels in each ROI was computed in power for the 43 images in all available polarizations. Plots showing the average coefficient evolution for each class, incidence angle and polarization along the hydrologic year 2006–2007 were drawn and are presented in the next section in dB units. HH and VV backscattering ratios were also graphed, in order to analyze the polarimetric behavior of the land cover types.

5. Results and discussion

In the following subsections, observations about the different land cover types backscattering characteristics before, during and after the inundation are presented.

5.1. Land cover type: deep bare soil

Deep Bare Soil ROIs consist of either even clayey soil, when they are emerged, or open water, when inundated. The dominant backscattering mechanism in both cases is surface scattering. Consistently with this mechanism, the temporal signatures of this class show higher σ^0 in VV than in HH polarization at all swaths both before and after the inundation. A linear regression of σ^0HH (dB) versus σ^0VV (dB) including all Deep Bare Soil data in the six ASAR incidence angles showed a slope $\Delta\sigma^0$VV/$\Delta\sigma^0$HH of 0.92 with an $R^2 = 0.93$.

The ROIs of the class Deep Bare Soil were emerged in only 8 of the 43 ASAR images, at swaths IS1, IS3, IS4 and IS6. In virtually all cases the backscattering coefficient of the emerged bare soil was higher than that from the flooded surface at the same swath and polarization (Fig. 5a, b, c).

When the Deep Bare Soil ROIs are flooded, their backscattering is highly dependant on the wind-induced surface roughness at steep incidence angles (Brown et al., 1996; Henderson & Lewis, 1998; Kandus et al., 2001; Leconte & Pultz, 1991; Töyrä et al., 2001). Backscattering values have been compared with the wind velocity averaged for the 6 h prior to each image acquisition, which is the wind responsible for the water surface roughness at that time. The results showed that above a mean wind velocity of about 1.5 m/s there is a positive correlation between wind speed and σ^0 at swaths IS2, IS3 and IS4 (there are not enough data at IS1). Fig. 5a and b illustrates this correlation.
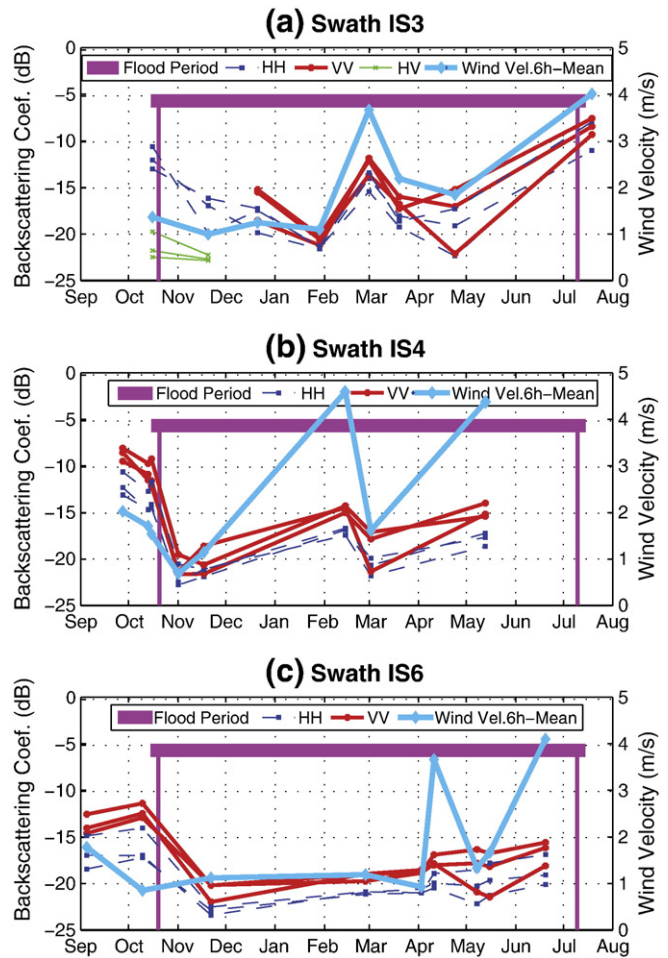

Fig. 5. Deep Bare Soil ROIs σ^0HH and σ^0VV evolution during the 2006–2007 hydrologic cycle at swaths IS3 (a), IS4 (b) and IS6 (c). Wind velocity averaged for the 6 h prior to each image acquisition is also represented.

Under low wind conditions the open water σ^0 is very small, often below the ASAR noise equivalent σ^0, which can be explained by the fact that the incident radar beam is specularly reflected away from the sensor by the smooth water surface. Large incidence angles of swaths IS6 and IS7 also induce high amount of specular reflection (Brown et al., 1996; Henderson & Lewis, 1998; Kandus et al., 2001; Leconte & Pultz, 1991; Töyrä et al., 2001). Thus, backscattering at these swaths is generally low (under −15 dB) and less sensitive to wind speed than swaths IS2 to IS4 (Fig. 5c).

Backscattering differences between emerged and flooded Deep Bare Soil have been found to be lower in HH than in VV polarization. The minimum observed σ^0HH change before and after the inundation is lowest at IS1 and IS6. The smallest σ^0 difference at IS1 was observed on a windy day and can be explained by the high sensitivity of steep incidence angles to the water surface roughness. In the case of IS6 images, the shallow incidence angle causes high amount of specular reflection of the radar beam not only on the open water but also on the smooth bare clayey soil. Therefore, the σ^0 differences and, hence, the separability between emerged and flooded surface are smaller at IS1 and IS6 than at IS3 and IS4. Fig. 6 illustrates the separability of flooded versus emerged Deep Bare Soil at swaths IS3, IS4 and IS6.

The number of cross-polarized data is limited to 6 images at swaths IS1 and IS3. σ^0HV values are in all cases low or below the ASAR noise equivalent σ^0. The backscattering mechanism of the Deep Bare Soil class is surface scattering on a relatively smooth surface throughout the study period. This mechanism induces little
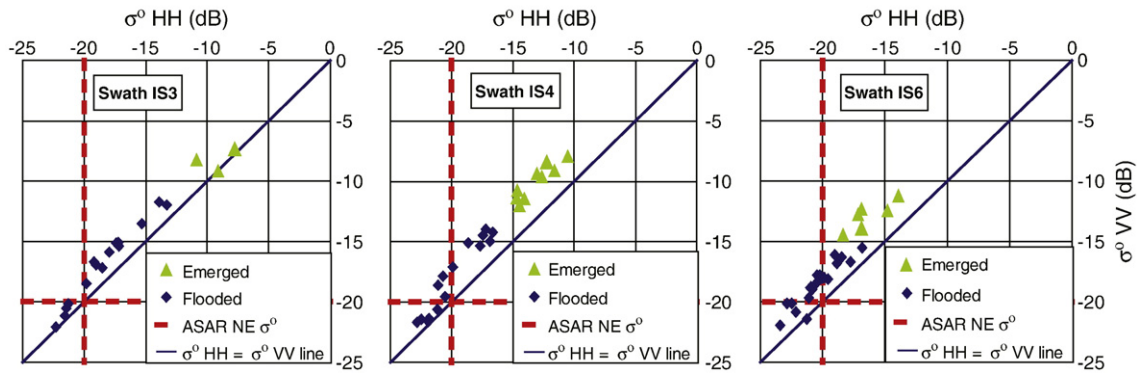
Fig. 6. Scatter plots of σ^0HH versus σ^0VV in the Deep Bare Soil ROIs at swaths IS3, IS4 and IS6.

depolarization of the electromagnetic radiation, which explains the low observed σ^0HV.

5.2. Land cover types: High Pacil and Low Pacil

The High Pacil ROIs did not flood during the study period, although they occasionally became swamped after strong rainfall events, such as the one on 28 January 2007, only a few hours before the IS3 image

acquisition on 29 January (Fig. 7c). The ROIs of class Low Pacil were flooded approximately from 11 November 2006 to 10 May 2007.

Right after the summer the soil is very dry everywhere in the Pacil and the backscattering coefficients of Low and High Pacil are close to each other (Fig. 7). A similar backscattering temporal pattern is observed in the High Pacil ROIs for all swaths: σ^0HH and σ^0VV take their lowest values at the beginning of the hydrologic year, when the soil is dry. They rise during the marshes flooding period, due
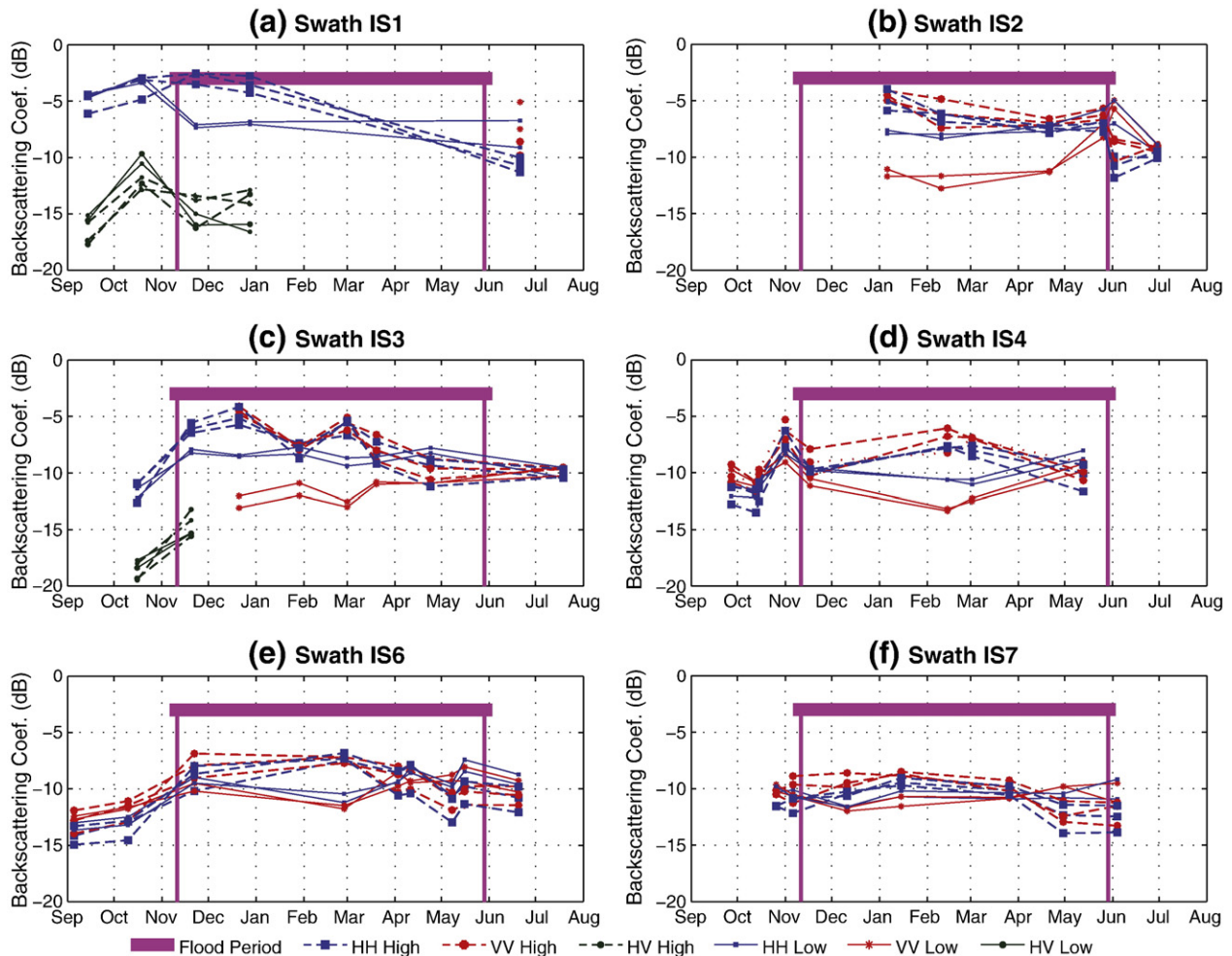

Fig. 7. High and Low Pacil ROIs σ^0HH and σ^0VV evolution during the 2006–2007 hydrologic cycle at swaths IS1, IS2, IS3, IS4, IS6 and IS7.
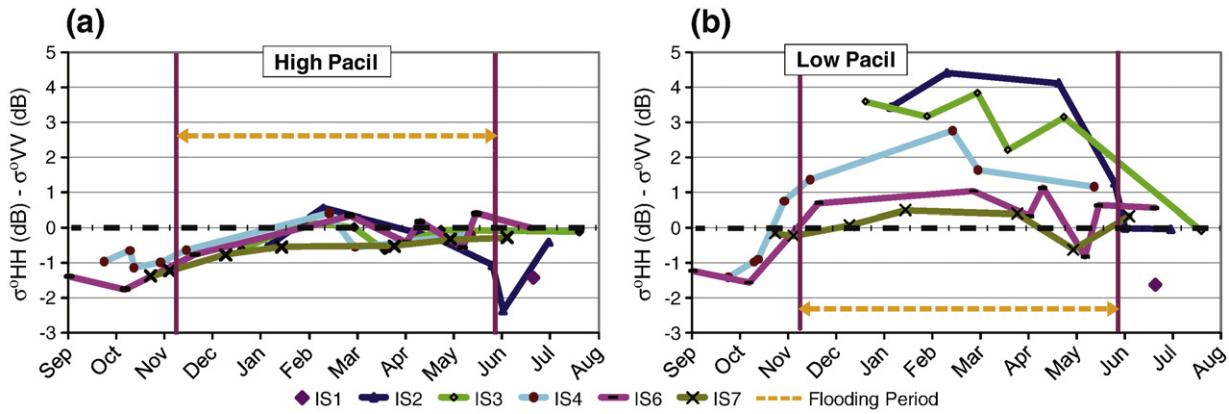
Fig. 8. High and Low Pacil ROIs σ^0HH/σ^0VV ratio evolution during the 2006–2007 hydrologic cycle at swaths IS1, IS2, IS3, IS4, IS6 and IS7.

presumably to the higher soil humidity, and go down again from April on, when the soil progressively dries out. The High Pacil ratio σ^0HH/σ^0VV shows a moderate increase during the flooding period at all swaths (Fig. 8a), and no significant effect of the incidence angle is observed on this parameter.

When the Low Pacil floods, σ^0 experiences a significant drop at swaths IS2, IS3 and IS4 with regard to those of the High Pacil (Figs. 7b, 7c, 7d, 9a and 9b), and this drop is more acute in VV than in HH. The σ^0 decrease could be explained by the lost of the surface scattering from bare soil and short pasture, which get covered by water and therefore induce forward reflection of the radar beam. A sound interpretation for the differential behavior between polarizations would be that double bounce is the dominant backscattering mechanism and that it is higher at HH than at VV polarization (Wang et al., 1995). This polarimetric response of the almajo would be explained by a preferential orientation of the almajo stems, but has not been explored yet.

At large incidence angles of swaths IS6 and IS7 polarimetric effects of the flooded Low Pacil signature are reduced (Figs. 7e, 7f, 8b and 9c). This could be explained by the fact that the path length through the almajo bushes increases and the direct volume backscattering mechanism becomes dominant.

Soon after the flooding period, in June, the ratio σ^0HH/σ^0VV of the Low and High Pacil takes again similar values (Fig. 8), but the backscattering coefficient from the Low Pacil is greater than that from the High Pacil (Fig. 7), presumably as a result of the rather higher humidity of the just unflooded soil.

5.3. Land cover types: Bayunco and Castañuela

Fig. 10 depicts the Bayunco and Castañuela ROIs backscattering signatures during the 2006–2007 hydrologic cycle. Five stages are

identifiable in these signatures, although images for at least one of the stages are missing at each swath. The stages depend on the ROIs water content (dry, wet, flooded) and the phenological phase of the vegetation (dry, green, density and emerging height). The five stages and the polarimetric multi-incidence angle radar response at each of them are discussed as follows:

Stage 1. In September, at the beginning of the hydrologic year, soil and vegetation are dry. Consistently with the reduced moisture content, the observed Bayunco and Castañuela backscattering is lower than in stages of wet soil or green emerged vegetation. Castañuela σ^0 ranges between −18 and −14 dB and Bayunco σ^0 between −16 and −11 dB at IS3, IS4 and IS6 (Fig. 10). The only available IS1 image in the same period shows σ^0 values substantially higher, in the order of −8 dB for the Castañuela and −5 dB for the Bayunco. This high backscattering at IS1 could be due, in large part, to the summer cloudburst that took place in the night, 11 h before the image acquisition, and that caused momentary soil and vegetation wetness.

Stage 2. From the beginning of the rainfall period, on 16 October 2006, until the inundation, in November, the Castañuela ROIs were permanently wet. The ASAR images in this period, at swaths IS1, IS4 and IS7, show backscattering values between −11 and −6 dB in the Castañuela ROIs, clearly higher than those for the previous dry soil stage (Fig. 10b1, b4, b6). The backscattering increment in this phase is assumed to be wetness-induced and is well illustrated by the IS4 temporal signature (Fig. 10b4). Bayunco regions flooded earlier than Castañuela regions and only one IS1 ASAR image was acquired between the beginning of the rainfall period and the inundation of two of the Bayunco
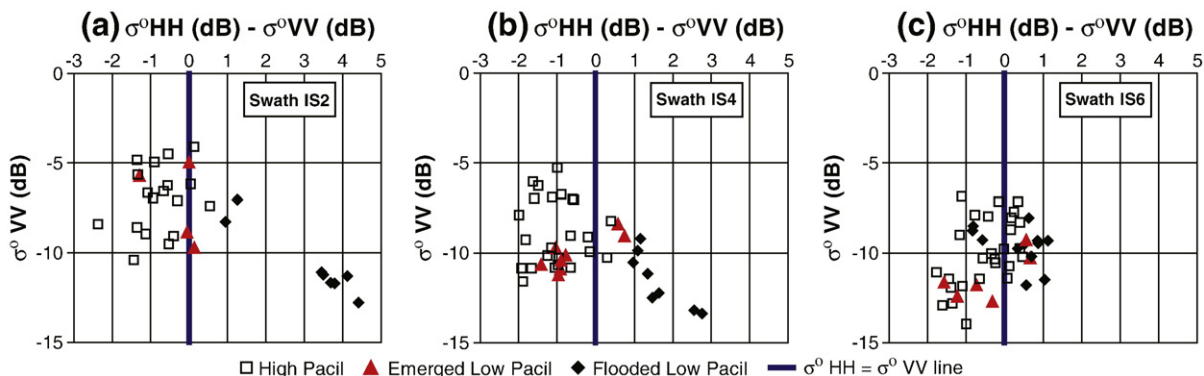

Fig. 9. Scatter plots of σ^0HH/σ^0VV ratio versus σ^0VV in the High and Low Pacil ROIs at swaths IS2, IS4 and IS6.
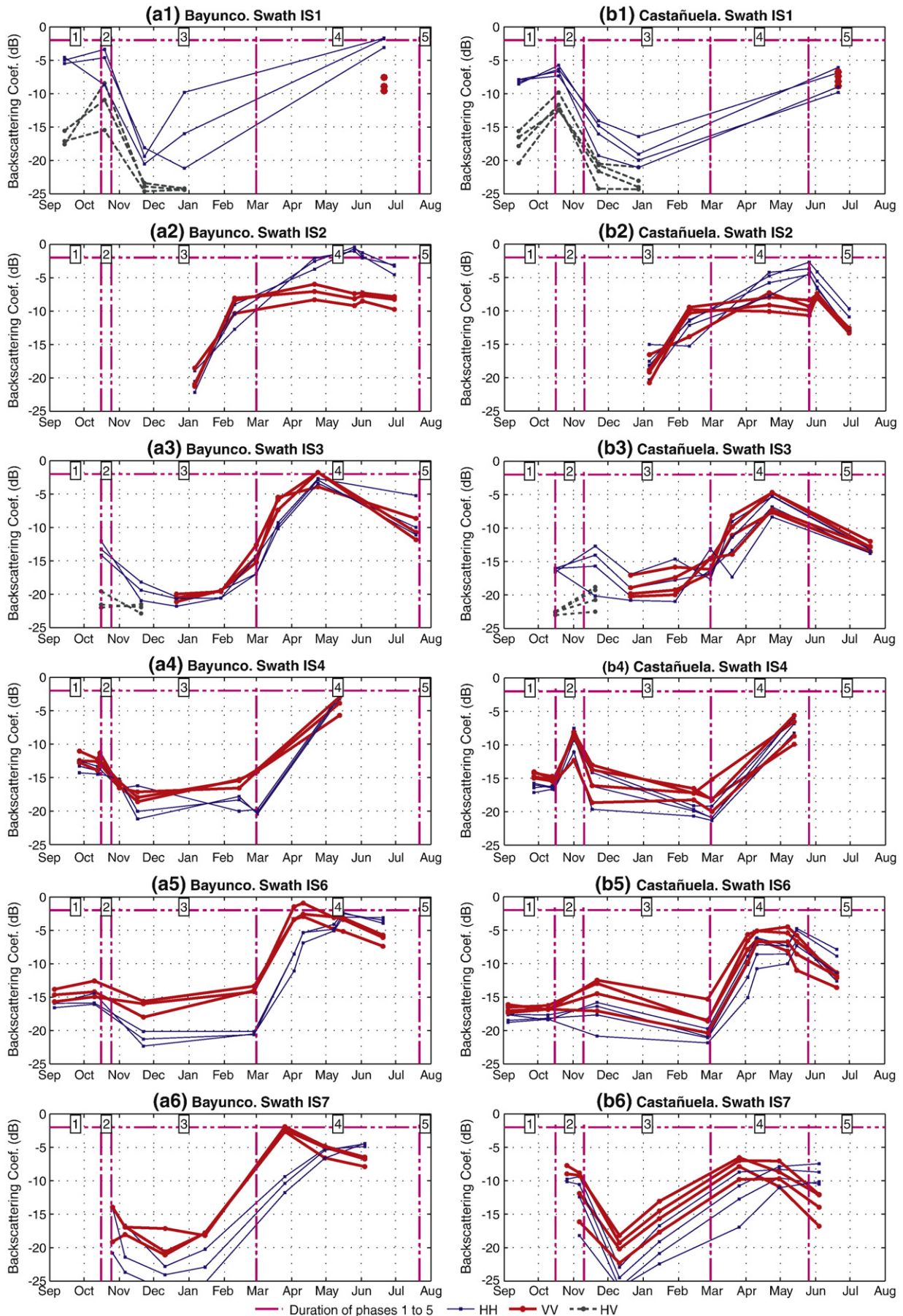
Fig. 10. Bayunco and Castañuela ROIs σ^0HH and σ^0VV evolution during the 2006–2007 hydrologic cycle at swaths IS1, IS2, IS3, IS4, IS6 and IS7.

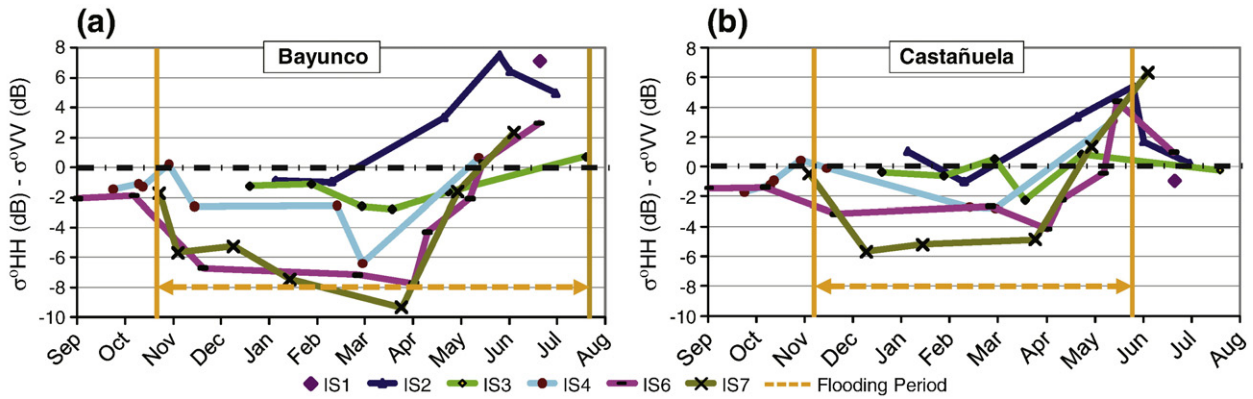**Fig. 11.** Bayunco and Castañuela ROIs σ^0HH/σ^0VV ratio evolution during the 2006–2007 hydrologic cycle at swaths IS1, IS2, IS3, IS4, IS6 and IS7.

ROIs (Fig. 10a1). Backscattering of the Bayunco ROIs at this second stage was about −4 dB, only 1 dB higher than in the previous stage, after a summer cloudburst.

Stage 3. Bayunco and Castañuela ROIs flooded approximately on 25 October 2006 and 6 November 2006, respectively. During this phase brown Bayunco and Castañuela stems stick out of the water surface in an amount dependant basically on the water depth and the time elapsed after the inundation (dry plants progressively putrefy and sink). A clear decrease in σ^0 is observed with respect to stage 2 at all swaths, which can be explained by the partial forward reflection of the radar beam on the water surface.

Castañuela regions show lower backscattering than in the previous stage of emerged wet soil at IS3, IS4 and IS7 (Fig. 10b), but similar to the first dry soil phase at IS3, IS4 and IS6 (no data are available to perform the same comparison at the rest of the swaths). Unlike the Castañuela, Bayunco backscattering in this stage is always lower than in the previous ones, especially at HH polarization (Fig. 10a).

It is worth mentioning that the Castañuela and Bayunco ROIs water surface remains rather smooth even on windy days, presumably as a result of the wind energy attenuation effect of the submerged vegetation. High backscattering from roughened water surface clearly distinguishes flooded bare soil from flooded Bayunco and Castañuela on windy days at this stage.

Stage 4. In March, new green Bayunco and Castañuela plants start coming out of the water and experience rapid height and density growth during the spring months, while the water level drops steadily. Concurrently, radar brightness shows a steep increase, reaching values 10 to 20 dB higher than in the previous stage (Figs. 10 and 13). Such increase might be explained by the specular double bounce of the radar waves between growing stalks and water surface, and by the vegetation canopy volume scattering. A clear swath dependant polarimetric behavior is observed in this stage:

- IS2 backscatter from flooded Bayunco and Castañuela is clearly higher in HH than in VV polarization (Fig. 10a2, b2). σ^0HH/σ^0VV increases at this swath with the plant growth reaching values above 7 and 5 dB for the Bayunco and Castañuela respectively. Bayunco σ^0VV reaches its maximum values around −7 dB in mid April, while σ^0HH continues to increase until the end of May, when it takes the highest values of about −0.6 dB. Backscattering from Castañuela follows the same temporal pattern: σ^0VV and σ^0HH maxima are achieved in mid April and end of May with approximate values of −9 and −5 dB, respectively.
- In contrast with swath IS2, Bayunco and Castañuela σ^0VV at IS6 and IS7 is higher than σ^0HH in March and April (Fig. 10a5,

a6, b5, b6). However, as it has been observed at IS2, σ^0VV reaches a maximum value and starts decreasing earlier than σ^0HH, so that the latter becomes greater than σ^0VV towards mid May. σ^0HH/σ^0VV increases in about 10 dB for both vegetation types in the course of this stage (Fig. 11).

- Polarimetric differences are lowest at swaths IS3 and IS4, but also in these cases σ^0VV is higher than σ^0HH in March and April (Fig. 10a3, a4, b3, b4). The imaging frequency at these swaths does not allow establishing a maxima time shift between polarizations, like for the rest of the incidence angles, although such maxima would fit the available data.

Strong differences between HH and VV backscattering, similar to the ones found in this study at swath IS2, were already spotted by Karszenbaum et al. (2000) and Grings et al. (2005) for flooded junco (i.e., reed-like vegetation comparable to the Bayunco), using ERS 2 (C band, VV polarization and 23° incidence angle), Radarsat S1(C-band, HH polarization and 23.5° incidence angle) and Envisat IS1 (C-band, HH/VV polarization and 19° incidence angle) data. Grings et al. explained through C-band electromagnetic model simulation that during the junco growing phase the HH backscattering dominates over the VV one, as observed for the Bayunco and Castañuela, due to three processes: 1) junco bistatic specular scattering is higher in the case of H incident polarization than in the V one; 2) water surface bistatic specular scattering is higher at H polarization than at V; 3) junco attenuation is higher at V than at H. In the simulations, both HH and VV responses increase with the junco growth due mainly to the water surface-stalks double bounce, up to a certain combination of vegetation height and density. Afterwards, further growth produces an increase in the attenuation and, hence, a decrease in σ^0. Their electromagnetic simulations also showed that during the junco growth the maximum σ^0 at 23° incidence angle was first achieved in VV polarization, consistently with this study's results. Grings et al.'s explanations of the junco backscattering behavior during the growing phase fit the observed Bayunco and Castañuela behavior in phase 4: σ^0 increases in virtue of the water-stalks double bounce up to a certain degree of plant development, after which the volume attenuation causes a decrease in σ^0VV. The orientation of the Bayunco and Castañuela stems, preferentially vertical, causes greater attenuation at VV radiation. As a result, σ^0VV starts decreasing for a smaller amount of emergent vegetation than σ^0HH. The fact that Bayunco polarimetric effects are larger than the Castañuela's might be explained

by the cylindrical shape and more vertical orientation of the first plant, which enhances the double bounce of the radar signal to a larger degree than the curved Castañuela leaves do (Grings et al., 2005; Grings et al., 2006).

A subsequent paper of the same authors, Grings et al., 2008, compared modeled σ^0HH and σ^0VV with ASAR signatures of flooded junco marshes at IS1 and IS3 incidence angles. Both, modeled simulations and experimental data showed that junco σ^0HH was clearly higher than σ^0VV at IS1 and IS3. In contrast, Doñana ASAR images show that σ^0HH at swaths IS3 to IS7 is lower than σ^0VV during most of the growing phase, and becomes only moderately higher at the end of the growing period, in May and June (Figs. 10 and 13). Such discrepancy should be due to the different vegetation type's geometries, such as emerged stem height, stem orientation or stem density. The Bayunco and Castañuela abrupt polarimetric behavior change between swaths IS2 and IS3, needs to be further investigated.

Stage 5. The Castañuela ROIs came out of water around 26 May 2007. A decrease of 3 to 7 dB in the total backscattering is observed at all swaths after the regions have emerged, except at swath IS7 and HH polarization (Fig. 10b). This decrease is probably due to the loss of water surface-stalks double bounce. At swaths IS6 and IS7, the HH backscattering coefficient, which had been smaller than the VV one all through the flooding stages 3 and 4, becomes now greater than the latter. At swath IS2 the σ^0HH/σ^0VV trend is opposite: it was clearly above 0 during stage 4 and drops abruptly to values around 0 (Fig. 11b) coinciding with the water's retreat. The same ratio is slightly affected at IS3, and remains with values close to 0 as in the previous stage.

The Bayunco ROIs came out of water between 6 and 26 July 2007. Despite the emerging time lag with respect to Castañuela, the same σ^0HH/σ^0VV trends on the same dates are observed (Fig. 11), suggesting that the HH and VV relative behavior at this phenological stage does not depend on the inundation but basically on the radar–vegetation interaction. Only in the last image, on 19 July at IS3, it is possible to observe two of the Bayunco ROIs out of water. Both HH and VV σ^0 in this image are 7 to 10 dB lower than in the previous IS3 image, acquired 3 months earlier.

As mentioned before, HV data are limited to the beginning of the hydrologic year and to swaths IS1 and IS3. HV backscattering is below the ASAR noise equivalent σ^0 value in the two IS3 images. IS1 HV Bayunco and Castañuela σ^0 ranges between −20 and −15 dB in September, increases above −12 dB at the beginning of the rainy period, due to plant and soil moisture, and goes down below the ASAR noise equivalent σ^0 after the flooding.

Fig. 11 embodies the σ^0HH/σ^0VV evolution in the Bayunco and Castañuela ROIs through the five stages described above. It can be seen in this figure that the σ^0HH/σ^0VV ratio is swath dependant at all stages, decreasing for larger incidence angles until May, when the Castañuela and Bayunco reach their maximum above water height and density. Fig. 11 also reveals that polarimetric effects are lowest at IS3 and IS4 throughout the hydrologic cycle.

Despite the σ^0 differences related to incidence angle, polarization and vegetation structure, Fig. 10 shows a similar backscattering temporal pattern of Bayunco and Castañuela in all swaths. This pattern is sketched in Fig. 12.

Fig. 13 illustrates the separability among Bayunco and Castañuela stages based on the σ^0VV and σ^0HH/σ^0VV ratio space. Flood detection feasibility is discussed in the following subsections.

5.3.1. Flood delineation at the beginning of the flooding period

Delineating flooded Bayunco and Castañuela areas at the beginning of the flooding period is equivalent to discriminating the areas in
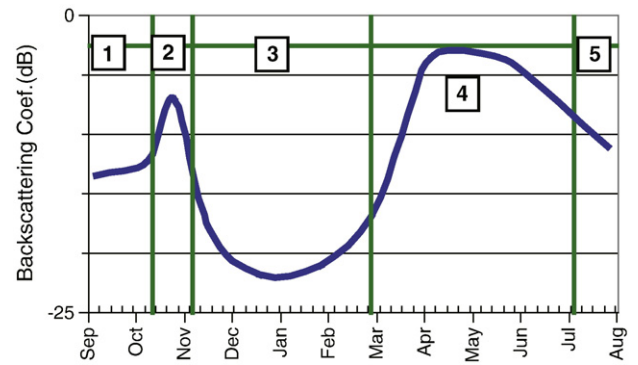

Fig. 12. Sketch of the temporal pattern and stages observed in the Bayunco and Castañuela backscattering signatures.

stage 3 from those still in stage 2. There are few observations of stage 2 ROIs in this study's results: only Castañuela ROIs at swaths IS1, IS4 and IS7 (Figs. 10b1, b4, b6 and 13b3, b5). In these observations the emerged and wet stage 2 areas show total backscattering of at least 5 dB higher than the flooded stage 3 ones. At swath IS7, backscattering decrease in stage 3 is accompanied by a shift in the σ^0HH/σ^0VV ratio (Fig. 13b5), which enhances the contrast between stage 2 and 3. Backscattering differences similar to the ones commented for IS4 and IS7 have been observed for Castañuela at swaths IS2 and IS6, although unfortunately in areas that were not part of the selected control ROIs, and therefore are not represented in the included figures. In the unlikely case of adjacent Castañuela areas at stage 1 (dry vegetation and soil) and stage 3 (flooded vegetation), their mean backscattering coefficient may be confounded, as illustrated by the very close stage 1 and stage 3 points in Fig. 13b.

Bayunco temporal signatures (Fig. 10a) show that at the beginning of the flooding period, HH backscattering from flooded Bayunco (stage 3) is clearly lower than that from the emerged plant (stages 1 or 2) in IS1, IS3, IS4 and IS6. Distinction is expected to be possible too at IS2 and IS7, since polarimetric effects and discrimination capacity are higher at these swaths than at IS3 and IS4. Fig. 13a shows that Bayunco stages 1 and 3 are close but still separable. Nevertheless, the distinction between emerged and flooded Bayunco is expected to be much clearer in the more likely case that areas at stage 3 are surrounded by others at stage 2 on the same ASAR image.

5.3.2. Flood delineation at the end of flooding period

Discrimination between flooded and emerged Bayunco and Castañuela regions at the end of the flooding period consists of discerning among areas at stages 4 and 5. According to Fig. 10b, a significant drop in the Castañuela backscattering coefficient takes place between both stages. So a clear contrast between flooded and emerged green Castañuela areas is to be expected at all swaths, the flooded ones being brighter. However, Fig. 13b1, b2 reveals that the reduced backscattering coefficient of the unflooded Castañuela regions at swaths IS2 and IS3 could be confounded with that from flooded areas with delayed plant development (e.g. at the middle of stage 4). No stage 5 data are available at IS4 (Fig. 13b3), but the minor polarimetric differences at this swath lead to expect an analogous drawback. At IS6 and IS7 incidence angles (Fig. 13b4, b5), a sustained increase in the HH/VV ratio along stage 4 prevents the confusion between stage 4 and 5 points.

Emerged green Bayunco was only observed on the last ASAR acquisition, at swath IS3. However, the more vertical orientation of this plant compared to that in Castañuela exacerbates the polarimetric effects which facilitate the discrimination of the inundation at IS6 and IS7 in the Castañuela case. So Bayunco flood mapping is expected
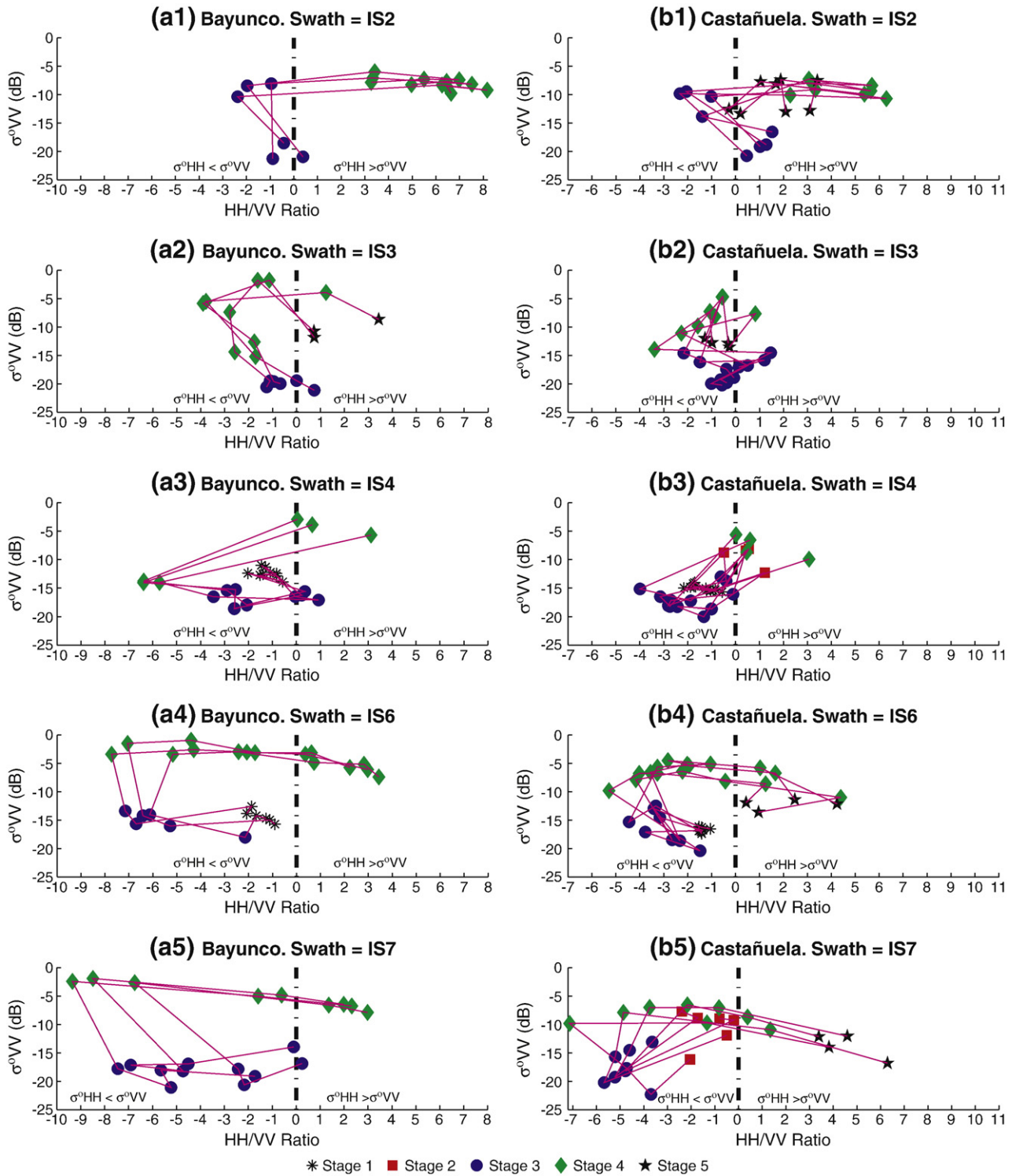
Fig. 13. Scatter plots of σ^0HH/σ^0VV ratio versus σ^0VV in the Bayunco (a) and Castañuela (b) ROIs at swaths IS2, IS3, IS4, IS6 and IS7. Point marker types indicate different stages. Points corresponding to the same ROI are connected by a polyline.

feasible at least at these swaths. Fig. 13a2 suggests that it could also be possible at IS3 and, by extension, at other swaths.

5.4. Combination of steep and shallow swaths

The discussion above refers to the flood detection feasibility on a single ASAR image. The versatility of the ASAR look direction allows observing Doñana at two different incidence angles with approximately 12 h delay, 6 times per 35-day orbit cycle. The following

combinations of 12 h-shifted observation swaths are possible twice per orbit cycle: IS1/IS6, IS3/IS4 and IS2/IS5. Provided the marshes flood state does not experience rapid changes in the period between scene acquisitions (e.g. rainfall occurs), both images can be combined for flood detection and, hence, benefit from the valuable additional information from two different look directions. This image composition is especially interesting when combining steep and shallow incidence angles, that is IS1/IS6 and IS2/IS5 pairs, since they provide more complementary information than the IS3 and IS4 closer swaths.
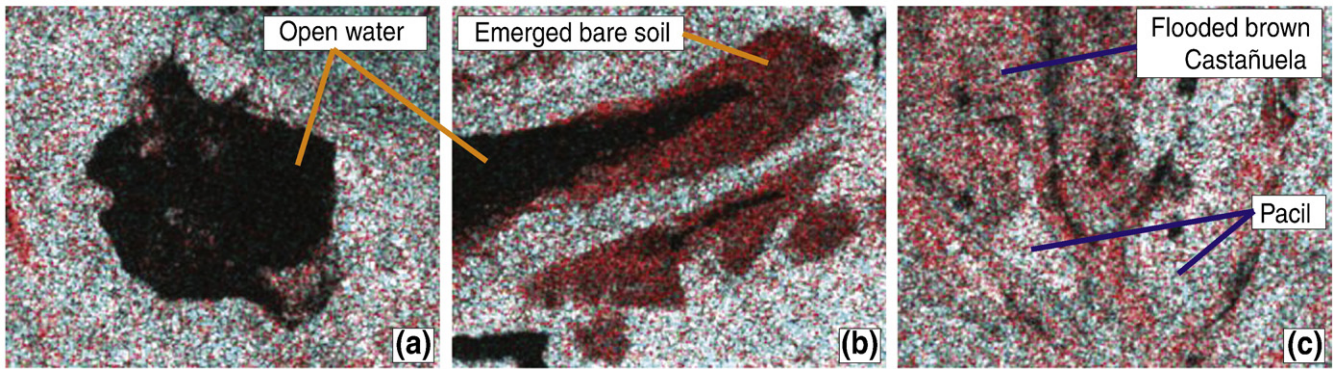
Fig. 14. Doñana marshes areas extracted from the IS6 HH/VV ASAR amplitude scene on 20 February 2008: a) flooded Deep Bare Soil pond; b) partially flooded Deep Bare Soil pond; c) flooded brown Castañuela. VV amplitude is displayed in red and HH in green and blue.

Fig. 15. Doñana marshes areas extracted from the IS1 HH/VV ASAR amplitude scene on 21 February 2008: a) flooded Deep Bare Soil pond; b) partially flooded Deep Bare Soil pond; c) flooded brown Castañuela. VV amplitude is displayed in red and HH in green and blue.
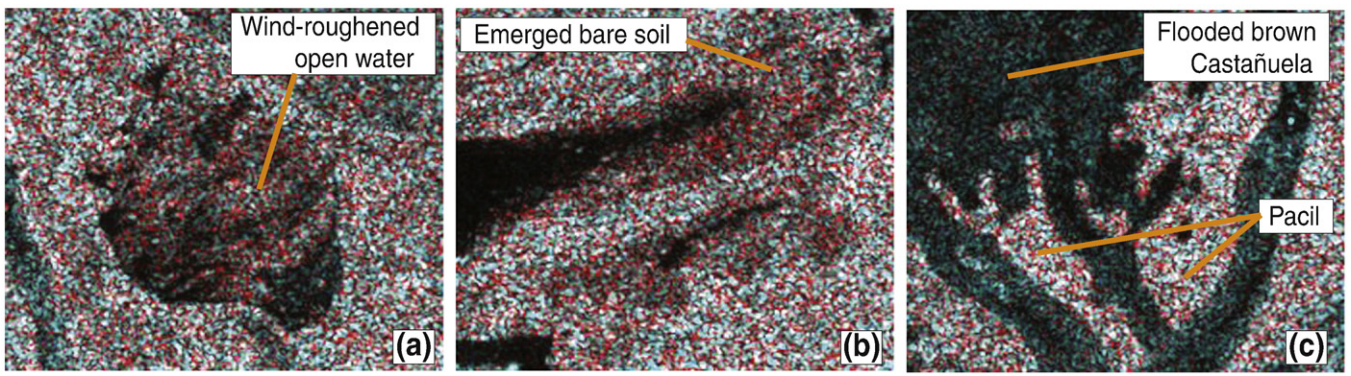
Figs. 14 and 15 show three zones in the marshes observed at swaths IS6 and IS1. They correspond to the IS6 and IS1 ASAR images acquired with 12 h and 14 min lag, as indicated in Table 2. These ASAR scenes do not belong to the study period analyzed in this article, but illustrate the advantage of combining swaths IS1 and IS6 with respect to the use of either of the same swaths independently.

Fig. 14a shows the extent of one flooded Deep Bare Soil pond with clarity. The extent of the same pond at IS1 (Fig. 15a) is less evident due to the increased backscattering from the roughened water surface, similar to that from the emerged bare soil in Fig. 16b. Flood and emerged bare soil are distinguishable at IS6 (Fig. 14a, b).

The area in Figs. 14c and 16c corresponds to brown Castañuela in shallow inundation. In this condition a significant volume of Castañuela sticks out of the water surface, but has lost vertical orientation compared to its young, green state. It yields high backscattering at IS6 (Fig. 14c), close to that from the same vegetation with emerged wet soil and close to that from the surrounding wet Pacil too. The same vegetation is more transparent at IS1, which shows low σ^0 values due to the water surface underneath, and therefore discerns the inundation from the adjacent Pacil more neatly (Fig. 15c). If flooded Pacil areas were present on the same ASAR scenes, IS1 would also be advantageous respect to IS6 in order to discriminate them, as discussed in Section 5.2.

Fig. 16 represents the following channel combination from the IS1 and IS6 ASAR scenes: IS6-VV is displayed in red, IS6-HH in green and IS1-VV in blue. This figure reveals how the inundation can be delineated in the three area types thanks to the quasi-simultaneous observation at two different incidence angles. The use of two different swaths shows potential, not only for flood mapping within a given land cover type, but also for discrimination among cover types in Doñana and therefore accounts for spatial distribution changes in them.

6. Conclusions

Conclusions on the flood mapping suitability of the various incidence angles for the different land cover types and phenological stages are presented as follows. These conclusions are currently being used to derive Doñana flood maps from ASAR images which, in turn, make possible the calibration of the marshes hydrodynamic model and to further the understanding of Doñana's complex hydrologic system.

6.1. Land cover type: deep bare soil

Deep bare soil temporal signatures and 2D scatter plots obtained in this study indicate that flooding stages are separable at swaths IS3 and IS4. High amount of specular reflection can cause confusion between flooded and emerged soil at large incidence angles. Confusion also

Table 2
Acquisition time, swath and polarization of the ASAR images in Figs. 14, 15 and 16.

Acquisition time	Swath	Polarization
20 February 2008, 22:26:43	IS6	HH/VV
21 February 2008, 10:40:45	IS1	HH/VV
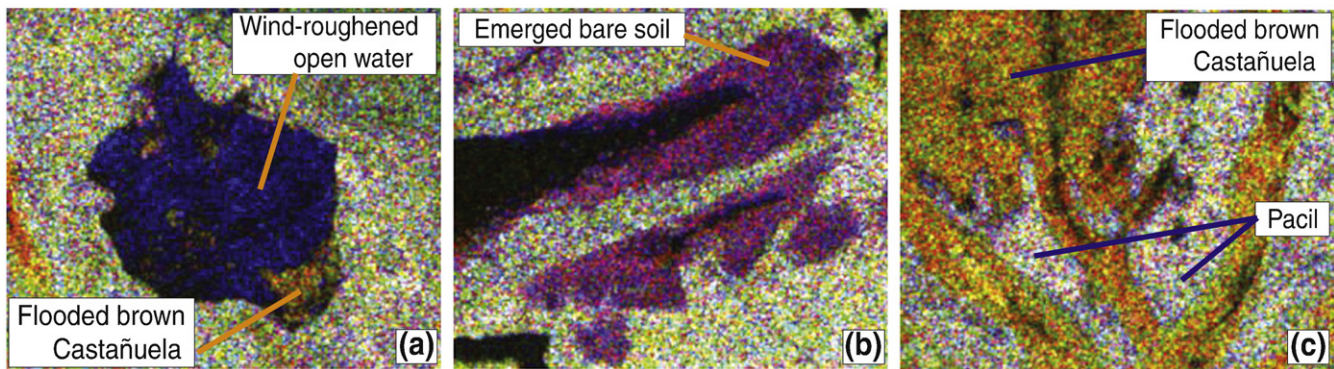
Fig. 16. Doñana marshes areas extracted from the IS6 and IS1 HH/VV ASAR amplitude scenes on 20 and 21 February 2008: a) flooded Deep Bare Soil pond; b) partially flooded Deep Bare Soil pond; c) flooded brown Castañuela. IS6 VV amplitude is displayed in red, IS6 HH in green and IS1 VV in blue.

occurs at steep incidence angles on windy days due to increased backscattering from wave action.

6.2. Land cover type: Low Pacil and High Pacil

Flooding in the Pacil is clearly detectable at swaths IS2, IS3 and IS4, and presumably at IS1 (there is not enough data at this swath). The indicators of this class inundation are a significant backscattering decrease in both polarizations and a steep increase in the σ^0HH/σ^0VV ratio, as a result of a larger drop at VV than at HH. The smaller the incidence angle the higher the σ^0HH/σ^0VV value and therefore the distinction of flooded versus emerged Pacil areas on a single image. At swaths IS6 and IS7 backscattering differences between flooded and emerged Pacil are subtle. Hence, when water levels in the marshes are high enough to reach Pacil areas, swaths IS6 and IS7 are not appropriate for flood mapping.

6.3. Land cover type: Bayunco and Castañuela

Flooded brown Castañuela can be discriminated at all incidence angles, except IS3, when the surrounding emerged regions are wet, because σ^0HH from the inundated areas is considerably lower than that from the emerged wet soil. There are no data for the same assertion about IS3. In the unlikely case of adjacent Castañuela areas of flooded and emerged dry soil, the inundation may not be separable. Delineating inundation in brown Bayunco areas is feasible at all swaths provided that HH data are available, since σ^0HH is always lower for flooded than for emerged brown Bayunco.

In spring and summer images, backscattering from green flooded Castañuela is substantially higher than that from the emerged plant at all swaths. However, certain confusion between emerged and low vegetated flooded areas can occur at IS2 and IS3. At IS6 and IS7 incidence angles the sustained increase in the HH/VV ratio at the end of the hydrologic year (Fig. 13b4, b5) prevents the same confusion. Although no data on unflooded green Bayunco ROIs are available, flood mapping is expected to be feasible at least at IS6 and IS7, because polarimetric effects enabling flood detection in the Castañuela case are more accused in the Bayunco areas.

In summary, virtually all single swaths can discern inundation at the beginning of the flooding period, while swaths IS6 and IS7 are preferred at the helophytes full development stage, towards the end of the hydrologic year. Additionally, in the particular case of the ASAR product used in this study, the IS6 and IS7 incidence angles have the advantage of a higher number of looks over steeper swaths and, therefore, less speckle than the latter.

Combination of 12 h-delayed ASAR images at steep and shallow incidence angles offers better flood detection capabilities than any single swath scene at all stages. Such acquisition combination is

possible at least 4 times in 35 days, which is a satisfactory observation frequency for Doñana flood extent monitoring. Future work aims at the utilization of these image pairs.

New satellite radar systems such as ALOS-PALSAR, RADARSAT-2 or TerraSAR-X provide fully polarimetric data, which has been proved to be advantageous for wetland monitoring (Boerner & Yamaguchi, 2008; Hong et al., 2010; Touzi, 2006; Touzi et al., 2009). Despite the doubtless added value data of these systems compared to the ASAR amplitude data used in this study, none of them can provide, in fully polarimetric mode, observations of the entire marshes at the temporal frequency achieved with ASAR. Both, temporal frequency and complete Doñana coverage were key requisites for this study's final goals.

References

Aragonés, D., Díaz-Delgado, R., & Bustamante, J. (2005, 21-23 Sep). Tratamiento de una serie temporal larga de imágenes Landsat para la cartografía de la inundación histórica de las marismas de Doñana. *Proceedings of the XI Congreso Nacional de Teledetección*. Tenerife, Spain: Asociación Española de Teledetección.

Bayán-Jardín, B., & Dolz-Ripollés, J. (1995). Las aguas superficiales y la marisma del Parque Nacional de Doñana. *Revista de Obras Públicas, 3340*, 17−29.

Bladé, E., & Gómez, M. (Eds.). (2006). *Modelación del flujo en lámina libre sobre cauces naturales. Análisis integrado en una y dos dimensiones. Monografía CIMNE, 97.* Barcelona, Spain: CIMNE.

Boerner, W. -M., & Yamaguchi, Y. (2008, 7-11 July). Recent advances in POL-SAR & POL-IN-SAR imaging of natural habitats and wetland remote sensing. *IEEE International Conference on Geoscience and Remote Sensing Symposium, 2.* (pp. 293−294)Boston, MA, U.S.A: IGARSS 2008.

Bourgeau-Chavez, l., Kasischke, E., Brunzell, S., Mudd, J., Smith, K., & Frick, A. (2001). Analysis of space-borne SAR data for wetland mapping in Virginia riparian ecosystems. *International Journal of Remote Sensing, 22*, 3665−3687.

Brown, R., Brisco, B., D'Iorio, M., Prevost, C., Ryerson, R., & Singhroy, V. (1996). RADARSAT applications: review of GlobeSAR program. *Canadian Journal of Remote Sensing, 22*, 404−419.

Bustamante, J., Pacios, F., Díaz-Delgado, R., & Aragonés, D. (2009). Predictive models of turbidity and water depth in the Doñana marshes using Landsat TM and ETM+ images. *Journal of Environmental Management, 90*, 2219—2225.

Cabezudo, B. (1979). Plantas de la reserva biológica de Doñana (Huelva). *Lagascalia, 8*, 167—181.

Clemente, L., García, L. V., Espinar, J. L., Cara, J. S., & Moreno, A. (2004). Las marismas del parque nacional de Doñana. *Investigación y Ciencia* (pp. 332)..

Costa, M. (2004). Use of SAR satellites for mapping zonation of vegetation communities in the Amazon floodplain. *International Journal of Remote Sensing, 25*, 1817—1835.

Costa, M., Novo, E., Ahern, E., Mitsuo, E. I. I., Mantovani, J., Ballester, M., et al. (1998). The Amazon flood plain through Radar eyes: Lago Grande de Monte Alegre case study. *Canadian Journal of Remote Sensing, 24*, 339—349.

Costa, M., & Telmer, K. (2006). Utilizing SAR imagery and aquatic vegetation to map fresh and brackish lakes in the Brazilian Pantanal wetland. *Remote Sensing of Environment, 105*, 204—213.

Díaz-Delgado, R., Bustamante, J., Pacios, F., & Aragonés, D. (2006, 19-20 Oct). *Hydroperiod of Doñana marshes: natural or anthropic origin of inundation regime? Proceedings of 1st GlobWetland Symposium: Looking at Wetlands from Space.* Frascati, Italy: ESA.

Dobson, M. C., Ulaby, F. T., Le Toan, T., Beaudoin, A., Kasischke, E. S., & Christensen, N. L., Jr. (1992). Dependence of radar backscatter on coniferous forest biomass. *IEEE Transactions on Geoscience and Remote Sensing, 30*, 412—415.

European Space Agency (2006). *ASAR Product Handbook*: ESA.

García, J. I., Mintegui, J. A., & Robredo, J. C. (2005). *La vegetación en la marisma del parque nacional de Doñana en relación con su régimen hidráulico.* Madrid, Spain: Ministerio de Medio Ambiente.

García-Novo, F., & Marín-Cabrera, C. (2005). *Doñana: agua y biosfera.* Madrid, Spain: Ministerio de Medio Ambiente.

Grings, F. M., Ferrazzoli, P., Jacobo-Berlles, J. C., Karszenbaum, H., Tiffenberg, J., Pratolongo, P., et al. (2006). Monitoring flood conditions in marshes using EM models and Envisat ASAR observations. *IEEE Transactions on Geoscience and Remote Sensing, 44*, 936—942.

Grings, F., Ferrazzoli, P., Karszenbaum, H., Tiffenberg, J., Kandus, P., Guerriero, L., et al. (2005). Modeling temporal evolution of junco marshes radar signatures. *IEEE Transactions on Geoscience and Remote Sensing, 43*, 2238—2245.

Grings, F., Ferrazzoli, P., Karszenbaum, H., Salvia, M., Kandus, P., Jacobo-Berlles, J. C., et al. (2008). Model investigation about the potential of C band SAR in herbaceous wetlands flood monitoring. *International Journal of Remote Sensing, 29*, 5361—5372.

Henderson, F. M., & Lewis, A. J. (1998). *Principles and applications of imaging radar.* Somerset, NJ: John Wiley and Sons, Inc..

Henderson, F. M., & Lewis, A. J. (2008). Radar detection of wetland ecosystems: A review. *International Journal of Remote Sensing, 29*, 5809—5835.

Hess, L., Melack, J., Filoso, S., & Wang, Y. (1995). Delineation of inundated area and vegetation along the Amazon floodplain with the SIR-C synthetic aperture radar. *IEEE Transactions on Geoscience and Remote Sensing, 33*, 896—904.

Hess, L., Melack, J., & Simonet, D. (1990). Radar detection of flooding beneath the forest canopy: A review. *International Journal of Remote Sensing, 11*, 1313—1325.

Hong, S. -H., Wdowinski, S., & Kim, S. -W. (2010). Evaluation of TerraSAR-X observations for wetland InSAR application. *IEEE Transactions on Geoscience and Remote Sensing, 48*, 864—873.

Ibáñez, E., & Gili-Ripoll, J. (2008). Validación de modelos digitales del terreno de precisión a partir de datos láser escáner aerotransportado; aplicación a la marisma del parque nacional de Doñana. PhD Thesis, Universitat Politècnica de Catalunya, Barcelona, Spain.

Kandus, P., Karszenbaum, H., Pultz, T., Parmuchi, G., & Bava, J. (2001). Influence of flood conditions and vegetation status on the radar backscatter of wetland ecosystems. *Canadian Journal of Remote Sensing, 27*, 651—662.

Karszenbaum, H., Kandus, P., Martinez, J. M., Toan, T. L., Tiffenberg, J., & Parmuchi, G. (2000, 16 – 20 Oct). ERS-2, RADARSAT SAR backscattering characteristics of the Paraná River delta wetlands, Argentina. *Proceedings of the ERS-ENVISAT symposium. Looking down to Earth in the new millennium.* Gothemburg, Sweden: ESA.

Kasischke, E., Melack, J., & Dobson, M. (1997). The use of radars for ecological applications: A review. *Remote Sensing of Environment, 59*, 141—156.

Kasischke, E., Smith, K., Bourgeau-Chavez, L., Romanowicz, E., Brunzell, S., & Richardson, C. (2003). Effects of seasonal hydrologic patterns in south Florida wetlands on radar backscatter measured from ERS-2 SAR imagery. *Remote Sensing of Environment, 88*, 423—441.

Krohn, D. M., Milton, N. M., & Segal, D. B. (1983). SEASAT synthetic aperture radar (SAR) response to lowland vegetation types in eastern Maryland and Virginia. *Journal of Geophysical Research, 88*, 1937—1952.

Le Toan, T., Beaudoin, A., Riom, J., & Guyon, D. (1992). Relating forest biomass to SAR data. *IEEE Transactions on Geoscience and Remote Sensing, 30*, 403—411.

Le Toan, T., Ribbes, F., Wange, L. F., Floury, N., Ding, N., & Kong, K. H. (1997). Rice crop mapping and monitoring using ERS-1 data based on experiment and modeling results. *IEEE Transactions on Geoscience and Remote Sensing, 35*, 41—56.

Leconte, R., & Pultz, T. (1991). Evaluation of the potential of Radarsat for flood mapping using simulated satellite SAR imagery. *Canadian Journal of Remote Sensing, 17*, 241—249.

Luque, C. J., Rubio-Casal, A. E., Álvarez, A. A., Muñoz, J., Vecino, I., Doblas, D., et al. (2005). *Memoria de Vegetación: Parque Nacional de Doñana. Proyecto de Cartografía y Evaluación de la Flora y Vegetación Halófita y de los Ecosistemas de Marismas que se encuentran dentro de la Red de Espacios Naturales Protegidos de Andalucía.* Sevilla, Spain: Consejería de Medio Ambiente de la Junta de Andalucía & Universidad de Sevilla.

Martí-Cardona, B., Dolz-Ripollés, J., & Gili-Ripoll, J. (2006, 19-20 Oct). Monitoring of the flooding and dry-out processes in Doñana National Park for the calibration of the hydrodynamic model of its marshes. *Proceedings of 1st GlobWetland Symposium: Looking at Wetlands from Space.* Frascati, Italy: ESA.

Martinez, J., & Le Toan, T. (2007). Mapping of flood dynamics and spatial distribution of vegetation in the Amazon floodplain using multitemporal SAR data. *Remote Sensing of Environment, 108*, 209—223.

Menanteau, L. (1984). Evolución histórica y consecuencias morfológicas de la intervención humana en las zonas húmedas: El caso de las marismas del Guadalquivir. *Las zonas húmedas en Andalucía* (pp. 43—76). Madrid, Spain: Dirección General de Medio Ambiente, Ministerio de Obras Públicas y Urbanismo.

Moreau, S., & Le Toan, T. (2003). Biomass quantification of Andean wetland forages using ERS satellite SAR data for optimizing livestock management. *Remote Sensing of Environment, 84*, 477—492.

Novo, E. M., Costa, M. F., & Mantovani, J. (1998). Exploratory survey on macrophyte biophysical parameters in tropical reservoirs. *Canadian Journal of Remote Sensing, 24*, 367—375.

Parmuchi, M., Karsenbaum, H., & Kandus, P. (2002). Mapping wetlands using multitemporal RADARSAT-1 data and a decision-based classifier. *Canadian Journal of Remote Sensing, 28*, 175—186.

Peinado, M., Martínez, J. M., Parras, C., Bartolomé, C., Álvarez, J., & De La Cruz, M. (1990). Nuevas plantas y nuevas áreas para la flora de Andalucía Occidenta. *Lagascalia, 16*, 125—129.

Pierdicca, N., Pulvirenti, L., & Bignami, C. (2010). Soil moisture estimation over vegetated terrains using multitemporal remote sensing data. *Remote Sensing of Environment, 114*, 440—448.

Pope, K., Rejmankova, E., Paris, J., & Woodruff, R. (1997). Detecting seasonal flooding cycles in marshes of the Yucatan peninsula with SIR-C polarimetric radar imagery. *Remote Sensing of Environment, 59*, 157—166.

Ramos, A., Martí-Cardona, B., Rabadà, J., & Dolz-Ripollés, J. (2009, 27-28 Oct). Teledetección e Información Hidrometeorológica de Campo en la Marisma de Doñana. *Proceedings of Jornadas de Ingeniería del Agua.* Madrid, Spain: CEDEX.

Ramsey, E. I. (1998). Radar remote sensing of wetlands. In R. Lunetta, & C. Elvidge (Eds.), *Remote sensing change detection: environmental monitoring methods and applications* (pp. 211—243). Chelsea, MI: Ann Arbor Press.

Ramsey, E., III (1995). Monitoring flooding in coastal wetlands by using radar imagery and ground-based measurements. *International Journal of Remote Sensing, 16*, 2495—2505.

Rivas-Martínez, S., Costa, M., Castroviejo, S., & Valdés-Bermejo, E. (1980). Vegetación de Doñana (Huelva, España). *Lazaroa, 2*, 5—189.

Rodríguez-Ramirez, A., & Clemente-Salas, L. (2002). Geomorfología. *Parque Nacional de Doñana* (pp. 19—42). Talavera de la Reina, Spain: Canseco Editores.

Rosenqvist, A., Forsberg, B., Pimentel, T., Rauste, Y., & Richey, J. (2002). The use of spaceborne radar data to model inundation patterns and trace gas emissions in the central Amazon floodplain. *International Journal of Remote Sensing, 23*, 1303—1328.

Rosich, B., & Meadows, P. (2004). *Absolute Calibration of SAR Level-1 Products Generated with PF-ASAR, v.1.4. ESA Technical Note*: ESA.

Saura, J., Bayán-Jardín, B., Casas, J., Ruíz, A., & Urdiales, C. (2001). *Documento marco para el desarrollo del proyecto Doñana 2005. Regeneración hídrica de las cuencas y cauces vertientes a las marismas del Parque Nacional de Doñana.* Madrid, Spain: Ministerio de Medioambiente.

Schmullius, C., & Evans, D. (1997). Synthetic aperture radar (SAR) frequency and polarization requirements for applications in ecology, geology, hydrology, and oceanography: A tabular status quo after SIR-C/X-SAR. *International Journal of Remote Sensing, 18*, 2713—2722.

Touzi, R. (2006, 31 July–4 Aug). Wetland characterization using polarimetric RADARSAT-2 capability. *IEEE International Conference on Geoscience and Remote Sensing Symposium, IGARSS 2006* (pp. 1639—1642). U.S.A: Denver, CO.

Touzi, R., Deschamps, A., & Rother, G. (2009). Phase of target scattering for wetland characterization using polarimetric C-band SAR. *IEEE Transactions on Geoscience and Remote Sensing, 47*, 3241—3261.

Töyrä, J., & Pietroniro, A. (2005). Towards operational monitoring of a northern wetland using geomatics-based techniques. *Remote Sensing of Environment, 97*, 174—191.

Töyrä, J., Pietroniro, A., & Martz, L. W. (2001). Multisensor hydrologic assessment of a freshwater wetland. *Remote Sensing of Environment, 75*, 162—173.

Ulaby, F. T., Moore, R. K., & Fung, A. K. (1986). *Microwave remote sensing: active and passive III. From theory to applications.* Norwood, MA: Artech House.

Wang, Y., Hess, L. L., Filoso, S., & Melack, J. M. (1995). Understanding the radar backscattering from flooded and nonflooded Amazonian forests: results from canopy backscatter modeling. *Remote Sensing of Environment, 54*, 324—332.

Wickel, A. J., Jackson, T. J., & Wood, E. F. (2001). Multitemporal monitoring of soil moisture with RADARSAT SAR during the 1997 Southern Great Plains hydrology experiment. *International Journal of Remote Sensing, 22*, 1571—1583.